J. Plasma Phys. (2025), *vol*. 91, E141 doi:10.1017/S0022377825100834

Bootstrap current modeling in M3D-C1

Saurabh Saxena[1,†], Nathaniel M. Ferraro[1], Mike F. Martin[2] and Adelle Wright[3]

[1]Princeton Plasma Physics Laboratory, Princeton, NJ, USA
[2]Thea Energy, Kearny, NJ 07032, USA
[3]University of Wisconsin–Madison, Madison, WI, USA

Corresponding author: Saurabh Saxena, ssaxena@pppl.gov

(Received 8 July 2025; revision received 14 August 2025; accepted 22 August 2025)

Bootstrap current plays a crucial role in the equilibrium of magnetically confined plasmas, particularly in quasi-symmetric stellarators and in tokamaks, where it can represent bulk of the electric current density. Accurate modeling of this current is essential for understanding the magnetohydrodynamic (MHD) equilibrium and stability of these configurations. This study expands the modeling capabilities of M3D-C1, an extended-MHD code, by implementing self-consistent physics models for bootstrap current. It employs two analytical frameworks: a generalized Sauter model (Sauter *et al.* 1999 *Phys. Plasmas* vol. **6**, no. 7, pp. 2834–2839), and a revised Sauter-like model (Redl *et al.* 2021 *Phys. Plasmas* vol. **28**, no. 2, pp. 022502). The isomorphism described by Landreman *et al.* (2022 *Phys. Rev. Lett.* vol. 128, pp. 035001) is employed to apply these models to quasi-symmetric stellarators. The implementation in M3D-C1 is benchmarked against neoclassical codes, including NEO, XGCa and SFINCS, showing excellent agreement. These improvements allow M3D-C1 to self-consistently calculate the neoclassical contributions to plasma current in axisymmetric and quasi-symmetric configurations, providing a more accurate representation of the plasma behavior in these configurations. A workflow for evaluating the neoclassical transport using SFINCS with arbitrary toroidal equilibria calculated using M3D-C1 is also presented. This workflow enables a quantitative evaluation of the error in the Sauter-like model in cases that deviate from axi- or quasi-symmetry (e.g. through the development of an MHD instability).

Key words: plasma simulation, fusion plasma, plasma instabilities

1. Introduction

Bootstrap current is a neoclassical electrical current in the plasma driven by inhomogeneities in the magnetic field and is proportional to temperature and density gradients in the plasma (Peeters 2000; Helander 2012). In tokamaks and quasi-symmetric stellarators, the bootstrap current can represent a significant fraction of the total current density, and it can strongly affect the rotational transform of the

[†]Present address: Thea Energy, Kearny, NJ, 07032, USA. Email: saurabh.saxena@thea.energy.

magnetic field (Helander, Geiger & Maaßberg 2011; Neuner *et al.* 2021). Therefore, accurate calculation of this current is essential for capturing corrections due to neoclassical physics.

Neoclassical transport can be calculated by solving the drift-kinetic equation. While several codes exist to solve this equation, obtaining a self-consistent state requires solving both the drift-kinetic equation and the magnetohydrodynamic (MHD) equilibrium equations iteratively (Landreman, Buller & Drevlak 2022). This process is computationally intensive (Redl *et al.* 2021). As a more efficient alternative, analytical models can be employed to approximate neoclassical transport. One such model is the approach taken by Sauter, Angioni & Lin-Liu (1999), which provides a local expression for the bootstrap current and neoclassical conductivity. In this model, the coefficients relating the bootstrap current to temperature and pressure gradients are obtained by fitting results from the codes CQL3D (Monticello 1993; Killeen *et al.* 2012) and CQLP (Sauter, Harvey & Hinton 1994) applied to a range of axisymmetric equilibria. This model, however, is known to be less accurate at higher electron collisionalities $\nu_e^* > 1$ limiting its applicability near the plasma edge (Koh *et al.* 2012; Landreman & Ernst 2012). The model relies on three neoclassical parameters: fraction of trapped particles f_t, collisionality ν^* and effective charge number Z_{eff}. To overcome these limitations, a revised version of the Sauter model, developed by Redl *et al.* (2021), utilizes the NEO code (Belli & Candy 2008; Belli & Candy 2011), a drift-kinetic solver for neoclassical steady-state solutions. The revised model offers enhanced accuracy and robustness across a broader range of collisionalities, extending its applicability beyond the limitations of the original Sauter model. Both the Sauter model and the Redl model have been extensively verified and tested in tokamak geometry.

However, these models are not generally applicable to stellarators because they are exclusively fit to calculations in axisymmetric geometry. A recent approach by Landreman *et al.* (2022) addresses this by exploiting the isomorphism between axisymmetric and quasi-symmetric configurations. This method allows the application of the Redl model to compute the bootstrap current in quasi-symmetric stellarators. Here, quasi-symmetry refers to the special condition in which the magnetic field strength $B = |B|$ exhibits continuous symmetry in a suitable coordinate system. Specifically, B depends only on the flux-surface label (ψ) and a linear combination of Boozer poloidal (θ) and toroidal angles (ζ), such that for an integer N representing the toroidal periodicity of the geometry, $B = B(\psi, \theta - N\zeta)$ (Landreman *et al.* 2022). This symmetry ensures conserved guiding-center motion analogous to that in axisymmetric fields (Landreman 2019).

Bootstrap current models have been implemented into nonlinear MHD models at various levels of fidelity. A heuristic model of the bootstrap response was implemented in NIMROD in order to model neoclassical tearing modes (Gianakon, Kruger & Hegna 2002). The Sauter model has been implemented into JOREK and has been applied to dynamical modeling of the H-mode pedestal during Edge-Localised Mode (ELM) cycles (Pamela *et al.* 2017). At higher fidelity, and potentially applicable to arbitrary geometry, are approaches in which the MHD equations are augmented and closed by the introduction of a kinetic equation for the non-Maxwellian contributions to the distribution function (Wang & Callen 1992; Ramos 2010, 2011). Progress has been made in developing these models (Held *et al.* 2004; Lyons, Jardin & Ramos 2015) and implementing them into nonlinear MHD codes (Held *et al.* 2015), but they remain extremely computationally expensive and, thus far, limited in their application.

https://doi.org/10.1017/S0022377825100834 Published online by Cambridge University Press

Challenges remain in integrating these advances into comprehensive simulation frameworks, and there is still a notable gap in the ability of nonlinear MHD simulation codes to treat stellarators. Most MHD codes assume axisymmetric computational domains and are designed for tokamak applications and are only able to handle weakly shaped stellarator geometries (Schlutt *et al.* Schlutt et al., 2012, 2013; Roberds *et al.*, 2016). Recent advancements, however, have enabled M3D-C1 to model the nonlinear MHD evolution of strongly shaped stellarator plasmas by accommodating non-axisymmetric domain geometries (Zhou *et al.* 2021). The ability to treat stellarator geometry has also recently been implemented in JOREK3D (Nikulsin *et al.* 2022) and NIMSTELL (Carl & Brian 2021).

In this work, we further extend the capabilities of the M3D-C1 code to include self-consistent physics models for bootstrap current for both tokamak and quasi-symmetric stellarator geometry. For the calculation of bootstrap current, we use the Sauter *et al.* (1999) formula and its improved version described in Redl *et al.* (2021). Building on the method developed by Landreman *et al.* (2022), we apply isomorphism between axisymmetric and quasi-symmetric geometries to compute the bootstrap current for quasi-symmetric stellarator configurations.

The remainder of the paper is organized as follows. Section 2 provides an overview of the M3D-C1 code, including implementation details of the two bootstrap current models. This section also outlines the neoclassical models used for validation and verification. Section 3 details the computational set-up and presents results of cross-verification between M3D-C1 and the neoclassical models for a tokamak case and two quasi-axisymmetric stellarator cases. Additionally, this section presents simulations of the nonlinear evolution of a quasi-axisymmetric (QA) stellarator equilibrium, highlighting the impact of the bootstrap model. Finally, § 4 offers a summary of the findings and a discussion of their implications.

2. Model description

The M3D-C1 code is a high-fidelity extended-MHD code (Jardin *et al.* 2012*a*). It employs a split-implicit time scheme, which allows for time steps that extend beyond the Alfvénic time scale, enabling stable simulations on the transport time scale (Jardin 2012). The code utilizes high-order finite elements with C^1 continuity, constructed on an axisymmetric mesh. Recent developments have enabled M3D-C1 to model the MHD evolution of stellarator plasmas by accommodating non-axisymmetric domain geometries (Zhou *et al.* 2021). The governing equations for both tokamak and stellarator simulations are fully detailed in Jardin *et al.* (2012*a*) and Zhou *et al.* (2021), while the single-fluid model equations, relevant to the analysis of plasma behavior in this work, are reproduced in Appendix C.

In the present work, we extend M3D-C1 to include a non-inductive current source, specifically, the bootstrap current, by modifying Ohm's law as follows:

$$\boldsymbol{E} = -\boldsymbol{v}\times\boldsymbol{B} + \eta[\boldsymbol{J} - \boldsymbol{J}_x]. \tag{2.1}$$

Where, $\boldsymbol{E}$ is the electric field, $\boldsymbol{v}$ is fluid velocity, η is the electrical resistivity, and $\boldsymbol{J}$ is the current density. This is equivalent to adding a force on the electrons $\boldsymbol{F}^e_x$ such that $\boldsymbol{F}^e_x = -\eta\, n_e\, e\, \boldsymbol{J}_x$, which corresponds to removing the contribution of $\boldsymbol{J}_x$ to the friction force on the electrons due to collisions with ions (Braginskii 1965). Thus, collisional drag will cause the current density to decay towards $\boldsymbol{J}_x$. Even if the force is applied instantly, the actual current in the plasma $\boldsymbol{J} = \nabla\times\boldsymbol{B}/\mu_0$ will evolve on resistive time scales. How this force appears in the ion momentum equation depends

https://doi.org/10.1017/S0022377825100834 Published online by Cambridge University Press

on whether this is an internal force (e.g. the bootstrap current) or an external force (here, μ_0 is the permeability of free space). For an internal force, there must be an equal and opposite force in the ion momentum equation, which results in no net force added to the MHD force balance equation.

For a force consistent with a purely parallel, divergence-free current ($\boldsymbol{J}_x = J_\parallel(\boldsymbol{B}/B)$), the quantity $J_\parallel/B$ must remain constant on a magnetic surface. Using this condition, we can relate the local parallel current to the magnetic field via the expression

$$J_\parallel = \frac{\langle \boldsymbol{J}_x \cdot \boldsymbol{B} \rangle}{\langle B^2 \rangle} B, \tag{2.2}$$

where $\langle \cdot \rangle$ denotes the magnetic surface average. To calculate $\langle \boldsymbol{J}_x \cdot \boldsymbol{B} \rangle$, the generalized neoclassical models of Sauter *et al.* (1999) and Redl *et al.* (2021) are employed, which provide analytical expressions for this quantity. The specific forms of these models are given in Appendix A.

For stellarators, the bootstrap current is computed using the method introduced by Landreman *et al.* (2022) (shown in (2.3)), which exploits the isomorphism between axisymmetric and quasi-symmetric geometries

$$\langle \boldsymbol{J}_x \cdot \boldsymbol{B} \rangle = \frac{\tilde{G}}{\iota - N} \Bigg[L_{31} \left(p_e \frac{\partial \ln n_e}{\partial \psi_t} + p_i \frac{\partial \ln n_i}{\partial \psi_t} \right) + p_e (L_{31} + L_{32}) \frac{\partial \ln T_e}{\partial \psi_t} + p_i (L_{31} + \alpha L_{34}) \frac{\partial \ln T_i}{\partial \psi_t} \Bigg]. \tag{2.3}$$

Here, $\tilde{G}(\psi_t) = G + NI$, G is $\mu_0/2\pi$ times the poloidal current outside the flux-surface (ψ_t), I is $\mu_0/2\pi$ the toroidal current inside the flux-surface (ψ_t), ψ_t is toroidal flux per radian i.e. $\Psi_t = 2\pi\ \psi_t$, ι is the rotational transform, $p_{e/i}$, $n_{e/i}$, $T_{e/i}$ are the electron (ion) pressures, densities and temperatures and α, L_{31}, L_{32}, L_{34} are the bootstrap coefficients (see Appendix B for further definitions). The Sauter–Redl–Landreman formulation requires information about the global equilibrium, quantities such as G, I and ψ_t. This information is generally not known within M3D-C1, as its treatment of magnetic field does not assume the presence of magnetic surfaces. To address this challenge, a separate calculation is performed in which an approximate magnetic coordinate system is constructed from M3D-C1 output using Fusion-IO (Ferraro 2025), taking isotherms of T_e as proxies for magnetic surfaces. Due to the strongly anisotropic conduction of T_e, these isotherms closely coincide with magnetic surfaces when surfaces exist and the dynamics is sufficiently slow; when surfaces do not exist, the isotherms are related to quadratic flux minimizing surfaces (Dewar, Hudson & Price 1994). However, it is worth reiterating that the Sauter–Redl–Landreman formula is valid only in quasi-symmetric geometries. Limitations introduced by deviations from quasi-symmetry are discussed in § 3.2.

To evaluate the neoclassical bootstrap current density and its related coefficients correctly, it is necessary to compute quantities such as the trapped particle fraction f_t and geometric factors like the inverse aspect ratio ϵ and qR (as defined in Appendix B). These parameters are integral to the expressions for the bootstrap current coefficients α, L_{31}, L_{32} and L_{34} (see Redl *et al.* 2021 for detailed expressions). To facilitate these calculations, we define a coordinate system based on the electron temperature isotherms, $\hat{T}_e = 1 - T_e/T_e^{max}$ with T_e^{max} being the maximum electron temperature within the plasma domain. This is roughly analogous

https://doi.org/10.1017/S0022377825100834 Published online by Cambridge University Press

to the normalized flux $\Psi_{t_N} = \psi_t/\psi_{LCFS}$. Within this framework, the global equilibrium quantities $\langle I(\hat{T}_e)\rangle$, $\langle G(\hat{T}_e)\rangle$, $\langle \hat{T}_e\rangle$, along with $\langle f_t(\hat{T}_e)\rangle$, $\langle \epsilon(\hat{T}_e)\rangle$, $\langle qR(\hat{T}_e)\rangle$ and $\iota(\hat{T}_e) = (\mathrm{d}\Psi_p/\mathrm{d}\hat{T}_e)/(\mathrm{d}\Psi_t/\mathrm{d}\hat{T}_e)$ are calculated externally to M3D-C1 as flux-surface averages (all flux-surface averaging is performed externally). They are then read into M3D-C1 at the start of the simulation and extrapolated to local mesh coordinates. During the dynamical simulations, the bootstrap coefficients α, L_{31}, L_{32} and L_{34} are evaluated locally at each time step using the evolving profiles of $\hat{T}_e$. The global equilibrium quantities are re-extrapolated at the beginning of each time step to reflect the updated $\hat{T}_e$ distribution. Using $\hat{T}_e$ rather than T_e enables a consistent treatment of cases where the temperature profile evolves in amplitude but maintains its shape, thereby avoiding unnecessary recomputation of the global quantities and other variables required for the calculation of the bootstrap coefficients.

To validate the accuracy of the bootstrap current calculations in M3D-C1 simulations, the results are compared with predictions from well-established neoclassical codes, namely: (i) XGCa, a global total-f gyrokinetic neoclassical code, where f is the 5D phase space distribution function (see Hager & Chang 2016 for details), (ii) NEO, a drift-kinetic neoclassical steady-state solver, a detailed description of which can be found in Belli & Candy (2008, 2011) and (iii) the stellarator neoclassical code SFINCS (the stellarator Fokker–Planck iterative neoclassical conservative solver), which solves the radially local four-dimensional drift-kinetic equation without assuming quasi-symmetry. See Landreman *et al.* (2014) for further details. These comparisons are performed for both tokamak (NEO, XGCa, SFINCS) and quasi-symmetric stellarator (SFINCS) geometries, ensuring consistent and reliable results across a range of magnetic confinement configurations.

3. Numerical results: bootstrap current calculations

3.1. *Tokamak case verification*

For the verification study, the low aspect ratio 'CIRC1' case from Hager & Chang (2016) is considered here. The configuration features a circular cross-section with inverse aspect ratio $\epsilon = 0.84$ at the outer boundary. In this analysis, following Hager & Chang (2016), the inverse aspect ratio ϵ is defined as the ratio of the mean minor radius $a_{mean} = (R_{max} - R_{min})/2$ to the geometrical center $R_c = (R_{max} + R_{min})/2$ of a flux surface, where R_{max} and R_{min} are the maximum and minimum major radii on a flux surface. The density and temperature profiles used in the simulations are tanh-type pedestals, as shown in figure 1(*a*).

Figure 1(*b*) shows the bootstrap current profile for the CIRC1 configuration. Maximum bootstrap current occurs at $\psi_N \sim 0.89$, where $\epsilon = 0.63$ and the electron collisionality ν_e^* is 0.92. A comparison between the M3D-C1 code using the Sauter *et al.* (1999) model and the NEO code's Sauter model reveals a 2.18 % difference at the peak of the bootstrap current profile. Furthermore, the bootstrap current profiles from M3D-C1 and XGCa are nearly identical, with a difference of only 0.04 % at the peak. The M3D-C1 profile calculated using the Redl *et al.* (2021) model shows a 2.12 % difference from XGCa and a 1.01 % difference from SFINCS profiles at the peak. It is important to highlight that the electron collisionality in this configuration is less than unity ($\nu_e^* < 1$), which is within the regime where the Sauter and Redl models are expected to provide reasonable approximations. While no single code serves as a definitive reference, NEO and SFINCS solve the drift-kinetic equation directly and provide high-fidelity neoclassical transport calculations. Given the complexity of bootstrap current calculations, agreement within a few percent at the

https://doi.org/10.1017/S0022377825100834 Published online by Cambridge University Press

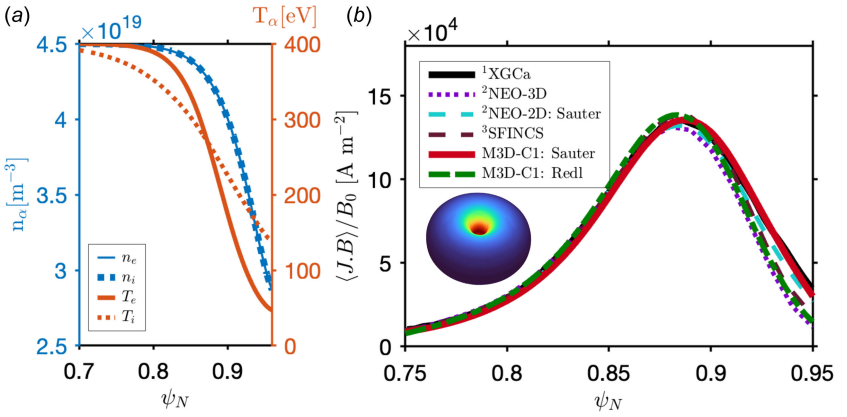

FIGURE 1. Set-up and results for tokamak verification: (*a*) prescribed density and temperature distributions; (*b*) bootstrap current profiles showing that M3D-C1 results closely approximate those from the drift-kinetic calculations. [1]Hager & Chang (2016), [2]Belli & Candy (2008, 2011), [3]Landreman *et al.* (2014).

profile peak is generally considered acceptable. Accordingly, the strong agreement among M3D-C1, NEO-3D, SFINCS and XGCa simulations supports the validity of the bootstrap current calculations for this case.

3.2. *Stellarator verification*

The implementation of Redl *et al.* (2021) formulae with the isomorphism as defined by Landreman *et al.* (2022) are verified on two QA stellarator configurations from Landreman & Paul (2022) and Landreman *et al.* (2022). These QA configurations both have a minor radius of 1.70 m and volume-averaged $B = 5.86$ T. The density (n) and temperature (T) profiles for both cases are specified using

$$n(\psi_{t_N}) = n_0\left(1 - \psi_{t_N}^5\right), \tag{3.1a}$$

$$T(\psi_{t_N}) = T_0\left(1 - \psi_{t_N}\right), \tag{3.1b}$$

where ψ_{t_N} is the normalized toroidal flux. For the first case (`QA_Case1`), a pure hydrogen plasma with $n_0 = n_{H,0} = 4.13 \times 10^{20}$ m^{-3} and $T_0 = T_{H,0} = 12$ keV (Landreman *et al.* 2022; Landreman *et al.* 2022 – § IV) is considered. This case uses a VMEC (Hirshman & Whitson, 1983) equilibrium with zero plasma pressure. VMEC is an equilibrium solver commonly used in stellarator optimization, which uses a variational method to find the minimum total energy of a system. The bootstrap current is calculated using the temperature and density profiles shown in figure 2(*a*), however, it is not self-consistent with the equilibrium. The second case (`QA_Case2`) is a QA configuration with $n_0 = n_{e,0} = 2.38 \times 10^{20}$ m^{-3}, $T_0 = T_{e,0} = 9.45$ keV, that was optimized for volume-averaged $\beta = 2.5$ % (see Sect. VIC in Landreman *et al.* 2022)). Here, β is the ratio of the plasma pressure to the magnetic pressure. Figures 2 and 3 provide further details of each configuration including the equilibrium profiles, cross-sections at various toroidal angles and three-dimensional views.

Figure 4 compares M3D-C1's bootstrap current profile with those of the SFINCS and Redl formulae from Landreman *et al.* (2022). It is evident from figure 4 that M3D-C1's implementation of the modified Redl *et al.* (2021) formulae, as presented

https://doi.org/10.1017/S0022377825100834 Published online by Cambridge University Press

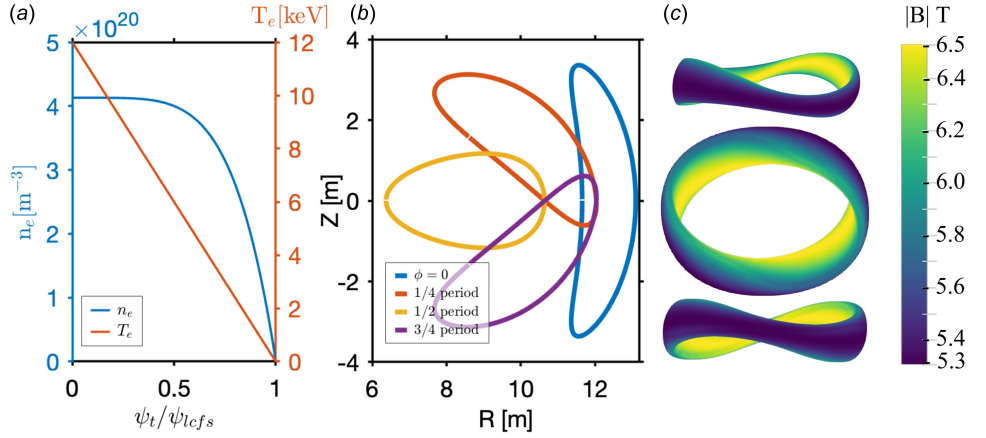

FIGURE 2. Quasi-axisymmetric configuration (`QA_Case1`): (*a*) density and temperature equilibrium profiles, (*b*) toroidal cross-sections of the plasma boundary and (*c*) three-dimensional view.

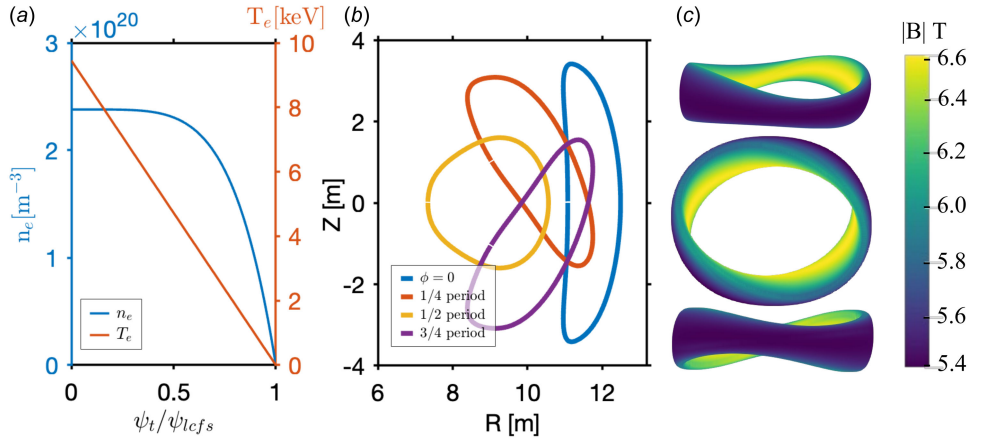

FIGURE 3. Optimized QA configuration with a volume-averaged $\beta = 2.5\,\%$ (`QA_Case2`): (*a*) density and temperature equilibrium profiles, (*b*) toroidal cross-sections of the plasma boundary and (*c*) three-dimensional view.

in Landreman *et al.* (2022), is in close agreement with the SFINCS and Redl based on calculations from Landreman *et al.* (2022). Minor discrepancies between the profiles may be attributed to numerical treatments between the codes or to temperature isotherms not being exactly aligned with the magnetic surfaces, although the exact sources remain unclear. Nevertheless, the results strongly support the robustness of M3D-C1's implementation in these complex configurations.

3.3. *Stellarator: nonlinear evolution*

In this section, the impact of the bootstrap model on the nonlinear evolution of a QA stellarator equilibrium is analyzed. The simulations conducted in M3D-C1 are initialized using the QA equilibrium profile from section VIC of Landreman *et al.*

https://doi.org/10.1017/S0022377825100834 Published online by Cambridge University Press

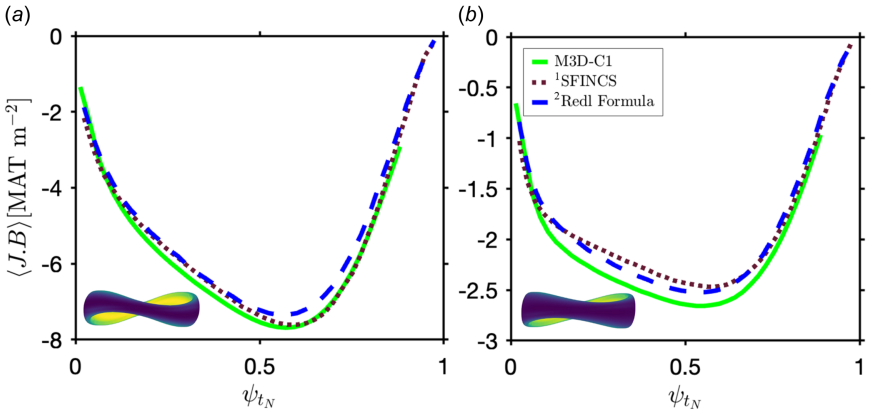

FIGURE 4. Bootstrap current profiles for (*a*) quasi-axisymmetric configuration (`QA_Case1`) and (*b*) optimized QA configuration with volume-averaged $\beta = 2.5\%$. (`QA_Case2`). [1]Landreman *et al.* (2014), [2]Redl *et al.* (2021).

(2022) (`QA_Case2`). The nonlinear evolution of the equilibrium are begun from an initial state with nested magnetic surfaces. This equilibrium, developed using SIMSOPT optimization software (Landreman *et al.* 2021), was optimized for low quasi-symmetry error, good energetic particle confinement and a self-consistent bootstrap current. The initial equilibrium profiles used in the simulations in this section are shown in figure 3(*a*). The computational domain is aligned with the shape of the equilibrium plasma, bounded by the last closed flux surface. The viscosity coefficient is fixed at ($\nu = 3.65 \times 10^{-4}$ kg (ms)$^{-1}$). The heat transport is modeled according to (C5), which accounts for thermal energy exchange and diffusion across the plasma. To explore a range of physical scenarios, several simulation configurations are examined. Four resistivity profiles are considered, using the Spitzer resistivity model with varying scaling factors of $\eta_0 = \{1, 10, 1000, 10\,000\}$. The general resistivity form is expressed as

$$\eta(R, \phi, Z) = \eta_{norm}\, \eta_0\, T_e^{-3/2}(R, \phi, Z), \tag{3.2}$$

where $\eta_{norm} = 2.74\ \Omega$m is the normalization factor for the classical resistivity value, η_0 is an artificial scale factor and T_e is the electron temperature at the position (R, ϕ, Z). In this set of simulations, the perpendicular thermal conductivity (κ) is held constant at 2.18×10^{-20} m^{-1} s^{-1}. To assess the effect of the bootstrap model, all configurations are evaluated with the bootstrap model both enabled and disabled.

The simulations are performed on a semi-structured grid consisting of 36 toroidal planes, resulting in a total of 1.88×10^5 three-dimensional elements within the computational domain. The grid is designed to provide sufficient resolution to accurately capture the nonlinear dynamics of the plasma.

Figure 5 shows the toroidal current density profiles from simulations with $\eta_0 = 10000$ at two times, $t = 0$ and $t = 250\tau_A$, comparing the cases with and without the bootstrap current model. In the absence of the bootstrap model, the current decays over time. In contrast, when the bootstrap model is enabled, the current is maintained, emphasizing its role in sustaining plasma currents. However, despite these differences, the simulations remain MHD unstable, and the current continues to evolve. The plasma instability is further evidenced by the Poincaré plots in figure 6. At $t = 250.0\tau_A$ in figure 6, these plots reveal that the chaotic region at the plasma

https://doi.org/10.1017/S0022377825100834 Published online by Cambridge University Press

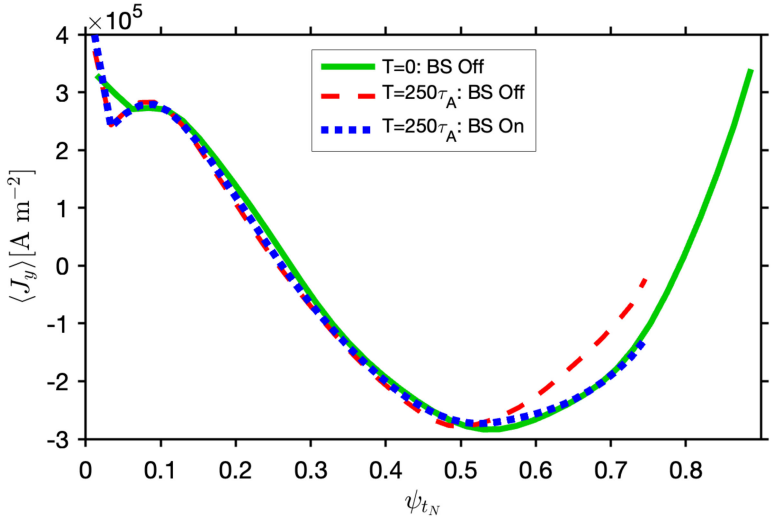

FIGURE 5. Toroidal current density profiles for simulations with resistivity scale factor $\eta_0 = 10^4$, comparing simulations with and without the bootstrap (BS) model at $t = 0$ and $250\tau_A$, highlighting the effect of the bootstrap current model on the profile evolution.

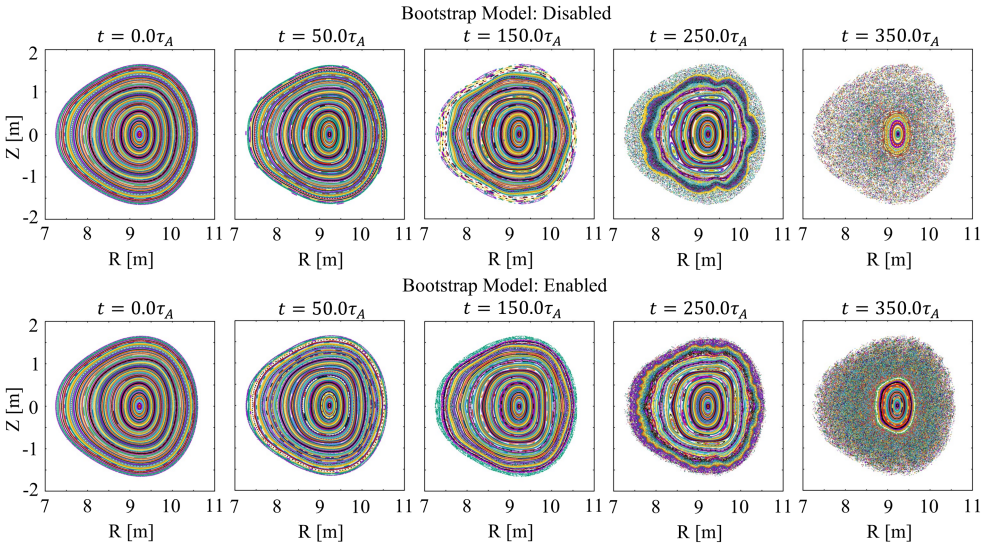

FIGURE 6. Poincaré sections of the magnetic field starting from a QA stellarator equilibrium optimized at 2.5 % plasma beta for the case with resistivity scale factor $\eta_0 = 10^4$ (`QA_Case2`). The sections are shown as a function of time for $0 \leq t \leq 350\tau_A$, comparing simulations with the bootstrap model disabled (top row) and enabled (bottom row).

boundary is significantly smaller when the bootstrap model is enabled, indicating that enabling the bootstrap model modifies the evolution of instabilities by slowing the breakup of magnetic surfaces.

It was found in Wright & Ferraro (2024*a*) that the growth of instabilities in equilibria similar to the ones under consideration here exist in the limit of low resistivity

https://doi.org/10.1017/S0022377825100834 Published online by Cambridge University Press

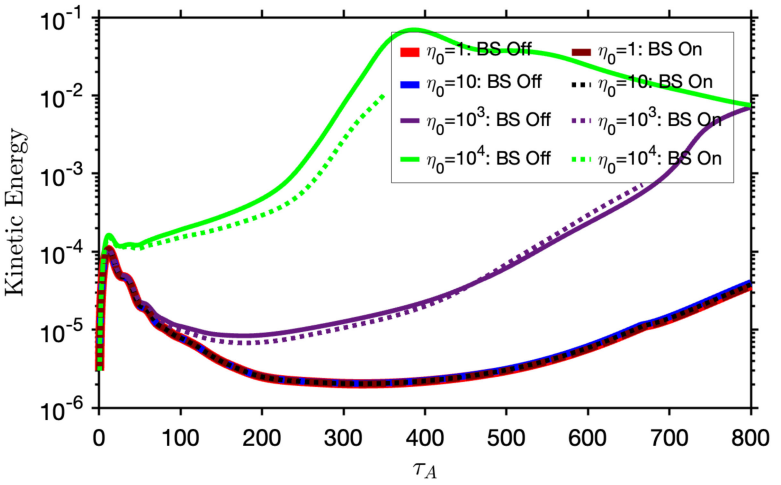

FIGURE 7. Time evolution of total kinetic energy for varying resistivity scaling factors $\eta_0 = 1$, 10, 1000 and 10 000 demonstrating faster kinetic energy growth at higher resistivity.

(e.g. are essentially ideal), but are accelerated at high resistivity. Because the instabilities progressed more rapidly than the resistive decay time, it was concluded that this result was not a consequence of neglecting the bootstrap current drive; for example, through the spurious resistive decay of equilibrium currents that are actually driven by the bootstrap effect. Now that we are in a position to evaluate this with a bootstrap model included, we vary the resistivity scaling factor η_0 here, running simulations with $\eta_0 = 1$, 10, 1000 and 10 000. Figure 7 shows the kinetic energy grows more rapidly with increasing resistivity, supporting the conclusions of Wright & Ferraro (2024*a*) that resistivity enhances the growth rate, even when the bootstrap model is included.

To further investigate the stability of the equilibrium over time, the deviation from quasi-symmetry is quantified as the system evolves. This is achieved by calculating the two-term quasi-symmetry error (F_{QS}) (Helander & Simakov 2008; Helander 2014; Paul, Antonsen & Cooper 2020), as shown in the following equation:

$$F_{QS} = \left\langle \left\{ \frac{1}{B^3} [(N - \iota M)\boldsymbol{B} \times \nabla B \cdot \nabla \psi - (MG + NI)\boldsymbol{B} \cdot \nabla B] \right\}^2 \right\rangle \tag{3.3}$$

where B is the magnetic field, $M = 1$, $N = 0$ for quasi-axisymmetry. The notation $\langle \cdot \rangle$ denotes the magnetic surface average, with isotherms of T_e serving as proxies for magnetic surfaces, consistent with the approach used in the bootstrap current calculation. Figure 8 compares F_{QS} obtained from M3D-C1 outputs with the bootstrap model enabled, at two distinct times $t = 0.0$, $t = 250.0\tau_A$, as well as from SFINCS and VMEC using the $t = 0$ equilibrium. The M3D-C1 F_{QS} metric closely resembles the VMEC quasi-symmetry error. While the equilibrium evolves over time, as observed in the Poincaré plots, the F_{QS} value does not significantly change in the range $0 < t < 250$ τ_A, indicating that quasi-symmetry is maintained throughout this period. However, beyond $t > 250$, the chaotic region grows, making it difficult to generate well-defined isothermal surfaces globally (at which point neoclassical transport is likely strongly subdominant to parallel transport along chaotic field lines anyway), so analysis is concluded there.

https://doi.org/10.1017/S0022377825100834 Published online by Cambridge University Press

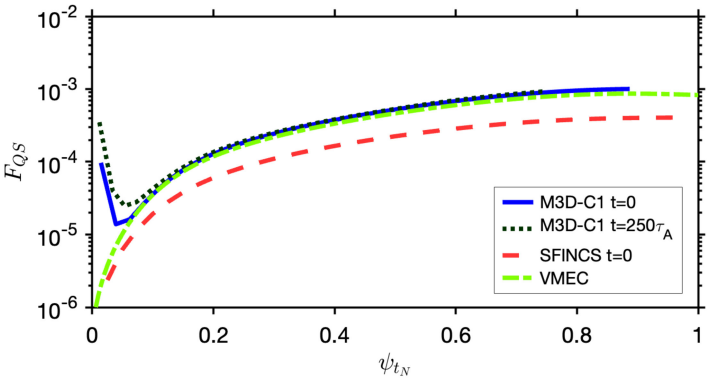

FIGURE 8. Two-term quasi-symmetry error as defined in (3.3) for the QA stellarator equilibrium optimized at 2.5 % plasma beta (`QA_Case2`) with a resistivity scale factor $\eta_0 = 10^4$.

4. Summary and discussion

This work enhances the capabilities of the M3D-C1 extended-MHD code by incorporating self-consistent bootstrap current models for tokamak and quasi-symmetric stellarator geometries. Two models are implemented, namely, (*a*) the Sauter model (Sauter *et al.* 1999) and (*b*) the Redl model (Redl *et al.* 2021). For quasi-symmetric stellarators, the isomorphism outlined by Landreman *et al.* (2022) is employed.

The numerical verification presented in this work demonstrates the accuracy of these new implementations. In § 3.1, the bootstrap current in a tokamak with a circular plasma boundary is tested using both bootstrap models. Comparisons between the flux-surface-averaged bootstrap current from the updated M3D-C1 code and results from established neoclassical codes, such as XGCa (Hager & Chang 2016), NEO (Belli & Candy 2008, 2011) and SFINCS (Landreman *et al.* 2014), show excellent agreement.

In § 3.2, the bootstrap current is evaluated in two quasi-symmetric stellarator configurations, `QA_Case1` and `QA_Case2`. These results are compared with SFINCS calculations, yielding good agreement. Finally, § 3.3 explores the application of the updated M3D-C1 code to nonlinear MHD simulations of an optimized QA stellarator configuration, where the expected toroidal current sustainment is observed.

The accurate modeling of bootstrap currents is critical to understanding and improving plasma performance in magnetic confinement devices. These results not only verify the bootstrap models in the updated M3D-C1 code but also highlight its potential to improve the design and optimization of future fusion reactors through accurate neoclassical current predictions in non-axisymmetric geometries. The successful implementation and verification of these models provides a solid foundation for advancing nonlinear MHD simulations, offering crucial insights that can guide the design and operational strategies of next-generation fusion devices.

This capability will enable new investigations into nonlinear MHD physics where bootstrap current is expected to be important. In particular, this includes transport-time scale simulations where the global equilibrium evolves due to heating, as is done in nonlinear calculations of pressure limits (cf. Wright & Ferraro 2024*b*), sawtooth cycles (cf. Jardin *et al.* 2012*b*) and ELM cycles (cf. Futatani *et al.* 2021), for example. While the implementation described here is only strictly valid for quasi-symmetric

https://doi.org/10.1017/S0022377825100834 Published online by Cambridge University Press

magnetic geometries, the ability to calculate the neoclassical transport of generic non-axisymmetric output using NEO 3D (Sinha *et al.* 2022, 2023) and SFINCS (as described above) enable *post hoc* evaluation of the accuracy of the Sauter–Redl–Landreman model. These capabilities also lay the groundwork for coupled M3D-C1/NEO 3D or M3D-C1/SFINCS modeling, which would be applicable to a wider range of geometries. One fundamental challenge is that the treatment of stochastic regions is beyond the scope of existing neoclassical theory, and requires a kinetic-MHD theory to treat self-consistently. In cases where the accuracy of the dynamics of these regions is less critical, such as when the time evolution is slow or time-dependent effects are negligible, the flattening of temperature and density profiles by classical transport along stochastic field lines, which is naturally included in the extended-MHD model, is expected to dominate over neoclassical effects in any case. We also note that the Sauter–Redl–Landreman models implemented here, as well as NEO 3D and SFINCS, all calculate time-independent transport, and are therefore not able to treat time-dependent neoclassical response. In principle this limits the applicability of the model on Alfvénic time scales (e.g. kink modes) – compounded by the fact that these modes are not likely to maintain quasi-symmetry – but the neoclassical response is not expected to play a significant role in such phenomena anyway.

Acknowledgements

Editor Per Helander thanks the referees for their advice in evaluating this article.

Funding

This work was supported by the U.S. Department of Energy under contract number DE-AC02-09CH11466. The United States Government retains a non-exclusive, paid-up, irrevocable, world-wide license to publish or reproduce the published form of this manuscript, or allow others to do so, for United States Government purposes.

Declaration of interests

The authors report no conflict of interest.

Data availability

The data that support the findings of this study are available from the corresponding author upon reasonable request.

Appendix A. Bootstrap current formulation

The bootstrap current formulation used in this study follows (A1) (Sauter *et al.* 1999; Sauter, Angioni & Lin-Liu 2002) and (A2) (Redl et al. 2021)

$$\langle \boldsymbol{J_x} \cdot \boldsymbol{B} \rangle = \langle j_\parallel B \rangle = -F(\psi) \left(p L_{31} \frac{\partial \ln p}{\partial \psi} + p_e L_{32} \frac{\partial \ln T_e}{\partial \psi} + p_i \alpha L_{34} \frac{\partial \ln T_i}{\partial \psi} \right), \quad \text{(A1)}$$

$$\langle \boldsymbol{J_x} \cdot \boldsymbol{B} \rangle = \langle j_\parallel B \rangle = -F(\psi) \left[p L_{31} \frac{\partial \ln n}{\partial \psi} + p_e (L_{31} + L_{32}) \frac{\partial \ln T_e}{\partial \psi} + p_i (L_{31} + \alpha L_{34}) \frac{\partial \ln T_i}{\partial \psi} \right], \quad \text{(A2)}$$

where $F(\psi) = R B_\phi$, ψ is poloidal flux per radian i.e. $\Psi_p = 2\pi\psi$, R is the major radius and B_ϕ the toroidal magnetic field. For details on the definitions of the coefficients in these equations, please refer to the corresponding references.

https://doi.org/10.1017/S0022377825100834 Published online by Cambridge University Press

For convenience, the common terms used to calculate the coefficients in (A1) and (A2) and their definitions, as presented in Sauter *et al.* (1999) and Redl *et al.* (2021) are summarized below.

The trapped particle fraction, denoted by f_t is

$$f_t = 1 - \frac{3}{4}\langle B^2\rangle \int_0^{1/B_{max}} \frac{\lambda \mathrm{d}\lambda}{\langle\sqrt{1-\lambda B}\rangle}. \tag{A3}$$

The effective electron and ion collisionalities are

$$\nu_e^* = 6.921\times 10^{-18}\frac{qRn_e \ln \Lambda_e}{T_e^2\varepsilon^{3/2}}, \tag{A4a}$$

$$\nu_i^* = 4.9\times 10^{-18}\frac{qRZ^4 n_e \ln \Lambda_{ii}}{T_i^2\varepsilon^{3/2}}. \tag{A4b}$$

The Coulomb logarithms are

$$\Lambda_e = 31.3 - \ln\left(\frac{\sqrt{n_e}}{T_e}\right), \tag{A5a}$$

$$\Lambda_{ii} = 30 - \ln\left(\frac{Z^3\sqrt{n_i}}{T_i^{3/2}}\right). \tag{A5b}$$

Here, R (m) is the major radius, $q = 1/\iota$ is the safety factor, with electron (T_e) and ion (T_i) temperatures in eV and densities (n_e and n_i) in m^{-3}.

Appendix B. Isomorphism

For applicability to quasi-symmetric stellarators, the Redl *et al.* (2021) formula is modified according to the isomorphism as defined in Landreman *et al.* (2022), see (2.3).

Noting that the rotational transform is defined as $\partial\psi/\partial\psi_t = \iota$, we have

$$\frac{\partial}{\partial\psi_t} = \iota\frac{\partial}{\partial\psi}. \tag{B1}$$

In the case of axisymmetry, $N = 0$ and $G = F = RB_\phi$ in (2.3) recovers the result of Redl et al. (2021). For the calculation of the bootstrap coefficients, the factors qR in (A4*a*) and (A4*b*) and the inverse aspect ratio ϵ are defined as follows:

$$qR = \frac{G + \iota I}{\iota - N}\left\langle\frac{1}{B}\right\rangle, \tag{B2a}$$

$$\epsilon = \frac{B_{max} - B_{min}}{B_{max} + B_{min}}. \tag{B2b}$$

Appendix C. M3D-C1: single-fluid equations

Summary of the M3D-C1 equations used in this study (reproduced from Jardin *et al.* (2012*a*))

$$\frac{\partial n}{\partial t} + \nabla\cdot(n\boldsymbol{v}) = 0, \quad \text{continuity}, \tag{C1}$$

$$nm_i\left(\frac{\partial \boldsymbol{v}}{\partial t} + \boldsymbol{v}\cdot\nabla\boldsymbol{v}\right) = \boldsymbol{J}\times\boldsymbol{B} - \nabla p - \nabla\cdot\boldsymbol{\Pi} + \boldsymbol{F}, \quad \text{momentum}, \tag{C2}$$

https://doi.org/10.1017/S0022377825100834 Published online by Cambridge University Press

$$\frac{\partial p}{\partial t} + \boldsymbol{v}\cdot\nabla p + \Gamma p \nabla\cdot\boldsymbol{v} = (\Gamma-1)[\eta J^2 - \nabla\cdot\boldsymbol{q} - \boldsymbol{\Pi}:\nabla\boldsymbol{v} + Q], \quad \text{energy},$$
$$= (\Gamma-1)[\eta \boldsymbol{J}\cdot(\boldsymbol{J}-\boldsymbol{J}_x) - \nabla\cdot\boldsymbol{q} - \boldsymbol{\Pi}:\nabla\boldsymbol{v} + Q] \tag{C3}$$

$$\frac{\partial \boldsymbol{B}}{\partial t} = \nabla\times(\boldsymbol{v}\times\boldsymbol{B} - \eta\boldsymbol{J})$$
$$= \nabla\times[\boldsymbol{v}\times\boldsymbol{B} - \eta(\boldsymbol{J}-\boldsymbol{J}_x)], \tag{C4a}$$

$$\boldsymbol{J} = \frac{1}{\mu_0}\nabla\times\boldsymbol{B}, \quad \text{Maxwell}, \tag{C4b}$$

$$\boldsymbol{q} = \kappa_\perp \nabla T_e - \kappa_\parallel \frac{\boldsymbol{B}\boldsymbol{B}}{B^2}\cdot\nabla T_e, \quad \text{heat transport model}, \tag{C5}$$

where n is the density, $\boldsymbol{v}$ is the fluid velocity, m_i is ion mass, $\boldsymbol{J}$ is the current density, $\boldsymbol{B}$ is the magnetic field, p is the pressure, $\boldsymbol{\Pi}$ is the viscous stress tensor, $\boldsymbol{F}$ is the external force, Q is external heat source, $\Gamma = 5/3$, η is the resistivity, $\boldsymbol{q}$ is the heat flux and μ_0 is the vacuum permeability. The viscous stress tensor is the sum of the ion and electron stress tensors $\boldsymbol{\Pi} = \boldsymbol{\Pi}_i + \boldsymbol{\Pi}_e$. The ion stress tensor has several contributing processes implemented following $\boldsymbol{\Pi}_i = \boldsymbol{\Pi}_i^\perp + \boldsymbol{\Pi}_i^\wedge + \boldsymbol{\Pi}_i^\parallel$, where $\boldsymbol{\Pi}_i^\perp$ is perpendicular ion viscosity, which represents the simple cross-field angular momentum diffusivity, $\boldsymbol{\Pi}_i^\wedge$ is the ion gyroviscosity, which represents the finite ion Larmor radius effects, and $\boldsymbol{\Pi}_i^\wedge$ is the parallel ion viscosity, representing the pressure anisotropy. The $\boldsymbol{\Pi}_e$ term is implemented as a hyper-resistive term.

REFERENCES

Belli, E. A. & Candy, J. 2008 Kinetic calculation of neoclassical transport including self-consistent electron and impurity dynamics. *Plasma Phys. Control Fusion* **50**, 095010.

Belli, E. A. & Candy, J. 2011 Full linearized Fokker–Planck collisions in neoclassical transport simulations. *Plasma Phys. Control Fusion* **54**, 015015.

Braginskii, S. I. 1965 Transport processes in a plasma. *Rev. Plasma Phys.* **1**, 205–311.

Carl, S. & Brian, S. 2021 Initial results of NIMSTELL, the stellarator variant of NIMROD. In *APS Division of Plasma Physics Meeting Abstracts, APS Meeting Abstracts*, vol. **2021**, pp. PP11.092.

Dewar, R. L., Hudson, S. R. & Price, P. F. 1994 Almost invariant manifolds for divergence-free fields. *Phys. Rev. A* **194**, 49–56.

Ferraro, N. M. 2025 Fusion-io, Available at: https://github.com/nferraro/fusion-io. Accessed 2025-05-08.

Futatani, S., Cathey, A., Hoelzl, M., Lang, P. T., Huijsmans, G. T. A. & Dunne, M.JOREK Team, the, ASDEX Upgrade Team, the & EUROfusion MST1 Team 2021 Transition from no-elm response to pellet elm triggering during pedestal build-upinsights from extended mhd simulations. *Nucl. Fusion* **61**, 046043.

Gianakon, T. A., Kruger, S. E. & Hegna, C. C. 2002 Heuristic closures for numerical simulations of neoclassical tearing modes. *Phys. Plasmas* **9**, 536–547.

Hager, R. & Chang, C. S. 2016 Gyrokinetic neoclassical study of the bootstrap current in the tokamak edge pedestal with fully non-linear coulomb collisions. *Phys. Plasmas* **23**, 042503.

Helander, P. 2012 Classical and neoclassical transport in tokamaks. *Fusion Sci. Technol.* **61**, 133–141.

Helander, P. 2014 Theory of plasma confinement in non-axisymmetric magnetic fields. *Rep. Prog. Phys.* **77**, 087001.

Helander, P., Geiger, J. & Maassberg, H. 2011 On the bootstrap current in stellarators and tokamaks. *Phys. Plasmas* **18**, 092505.

https://doi.org/10.1017/S0022377825100834 Published online by Cambridge University Press

HELANDER, P. & SIMAKOV, A. N. 2008 Intrinsic ambipolarity and rotation in stellarators. *Phys. Rev. Lett.* **101**, 145003.

HELD, E. D., CALLEN, J. D., HEGNA, C. C., SOVINEC, C. R., GIANAKON, T. A. & KRUGER, S. E. 2004 Nonlocal closures for plasma fluid simulations. *Phys. Plasmas* **11**, 2419–2426.

HELD, E. D., KRUGER, S. E., JI, J.-Y., BELLI, E. A. & LYONS, B. C. 2015 Verification of continuum drift kinetic equation solvers in nimrod. *Phys. Plasmas* **22**, 032511.

HIRSHMAN, S. P., & WHITSON, J. C. (1983). Steepest descent moment method for three-dimensional magnetohydrodynamic equilibria (No. ORNL/TM-8861). Oak Ridge National Lab. (ORNL), Oak Ridge, TN (United States). doi:10.2172/5537804

JARDIN, S. C. 2012 Review of implicit methods for the magnetohydrodynamic description of magnetically confined plasmas. *J. Comput. Phys.* **231**, 822–838.

JARDIN, S. C., FERRARO, N. M., BRESLAU, J. & CHEN, J. 2012*a* Multiple timesc*a*le calculations of sawteeth and other global macroscopic dynamics of tokamak plasmas. *Comput. Sci. Discov.* **5**, 014002.

JARDIN, S. C., FERRARO, N. M., BRESLAU, J. & CHEN, J. 2012*b* Multiple timescale calculations of sawteeth and other globle macroscopic dynamics of tokamak plasmas. *Comput. Sci. Discov.* **5**, 014002.

KILLEEN, J., KERBEL, G. D., MCCOY, M. G. & MIRIN, A. A. 2012 *Computational Methods for Kinetic Models of Magnetically Confined Plasmas*. Springer Science & Business Media.

KOH, S., CHANG, C. S., KU, S., MENARD, J. E., WEITZNER, H. & CHOE, W. 2012 Bootstrap current for the edge pedestal plasma in a diverted tokamak geometry. *Phys. Plasmas* **19**, 072505.

LANDREMAN, M. 2019 Quasisymmetry: a hidden symmetry of magnetic fields.

LANDREMAN, M., BULLER, S. & DREVLAK, M. 2022 Optimization of quasi-symmetric stellarators with self-consistent bootstrap current and energetic particle confinement. *Phys. Plasmas* **29**, 082501.

LANDREMAN, M. & ERNST, D. R. 2012 Local and global Fokker–Planck neoclassical calculations showing flow and bootstrap current modification in a pedestal. *Plasma Phys. Control Fusion* **54**, 115006.

LANDREMAN, M., MEDASANI, B., WECHSUNG, F., GIULIANI, A., JORGE, R. & ZHU, C. 2021 Simsopt: a flexible framework for stellarator optimization. *J. Open Source Softw.* **6**, 3525.

LANDREMAN, M. & PAUL, E. 2022 Magnetic fields with precise quasisymmetry for plasma confinement. *Phys. Rev. Lett.* **128**, 035001.

LANDREMAN, M., SMITH, H. M., MOLLÉN, A. & HELANDER, P. 2014 Comparison of particle trajectories and collision operators for collisional transport in nonaxisymmetric plasmas. *Phys. Plasmas* **21**, 042503.

LYONS, B. C., JARDIN, S. C. & RAMOS, J. J. 2015 Steady-state benchmarks of dk4d: a time-dependent, axisymmetric drift-kinetic equation solvera. *Phys. Plasmas* **22**, 056103.

MONTICELLO, D. A. 1993 Summary of the iaea technical committee meeting on advances in simulation and modeling thermonuclear plasmas. *Fusion Technol.* **23**, 362–363.

NEUNER, U., *et al.* 2021 Measurements of the parameter dependencies of the bootstrap current in the w7-x stellarator. *Nucl. Fusion* **61**, 036024.

NIKULSIN, N., RAMASAMY, R., HOELZL, M., HINDENLANG, F., STRUMBERGER, E., LACKNER, K., GÜNTER, S. & Team, JOREK 2022 Jorek3d: an extension of the jorek nonlinear mhd code to stellarators. *Phys. Plasmas* **29**, 063901.

PAMELA, S. J. P., *et al.* 2017 Recent progress in the quantitative validation of jorek simulations of elms in jet. *Nucl. Fusion* **57**, 076006.

PAUL, E. J., T. ANTONSEN Jr, LANDREMAN, M., COOPER, W. A. 2020 Adjoint approach to calculating shape gradients for three-dimensional magnetic confinement equilibria. Part 2. Applications. *J. Plasma Phys.* **86**, 905860103.

PEETERS, A. G. 2000 The bootstrap current and its consequences. *Plasma Phys. Control Fusion* **42**, B231.

RAMOS, J. J. 2010 Fluid and Drift-kinetic description of a magnetized plasma with low collisionality and slow dynamics orderings. I. Electron theory. *Phys. Plasmas* **17**, 082502.

RAMOS, J. J. 2011 Fluid and Drift-kinetic description of a magnetized plasma with low collisionality and slow dynamics orderings. II. Ion theory. *Phys. Plasmas* **18**, 102506.

REDL, A., *et al.* 2021 A new set of analytical formulae for the computation of the bootstrap current and the neoclassical conductivity in tokamaks. *Phys. Plasmas* **28**, 022502.

ROBERDS, N. A., GUAZZOTTO, L., HANSON, J. D., HERFINDAL, J. L., HOWELL, E. C., MAURER, D. A. & SOVINEC, C. R. 2016 Simulations of sawtoothing in a current carrying stellarator. *Phys. Plasmas* **23**, 092513.

SAUTER, O., ANGIONI, C. & LIN-LIU, Y. R. 1999 Neoclassical conductivity and bootstrap current formulas for general axisymmetric equilibria and arbitrary collisionality regime. *Phys. Plasmas* **6**, 2834–2839.

SAUTER, O., ANGIONI, C. & LIN-LIU, Y. R. 2002 Erratum: "neoclassical conductivity and bootstrap current formulas for general axisymmetric equilibria and arbitrary collisionality regime" [phys. plasmas 6, 2834 (1999)]. *Phys. Plasmas* **9**, 5140.

SAUTER, O., HARVEY, R. W. & HINTON, F. L. 1994 A 3-d Fokker-Planck code for studying parallel transport in tokamak geometry with arbitrary collisionalities and application to neoclassical resistivity. *Contrib. Plasm. Phys.* **34**, 169–174.

SCHLUTT, M. G., HEGNA, C. C., SOVINEC, C. R., HELD, E. D. & KRUGER, S. E. 2013 Self-consistent simulations of nonlinear magnetohydrodynamics and profile evolution in stellarator configurations. *Phys. Plasmas* **20**, 056104.

SCHLUTT, M. G., HEGNA, C. C., SOVINEC, C. R., KNOWLTON, S. F. & HEBERT, J. D. 2012 Numerical simulation of current evolution in the compact toroidal hybrid. *Nucl. Fusion* **52**, 103023.

SINHA, P., FERRARO, N. M. & BELLI, E. 2022 Neoclassical transport due to resonant magnetic perturbations in diii-d. *Nucl. Fusion* **62**, 126028.

SINHA, P., FERRARO, N. M. & BELLI, E. A. 2023 Neoclassical transport of impurities in tokamaks with non-axisymmetric perturbations. *Phys. Plasmas* **30**, 122506.

WANG, J. P. & CALLEN, J. D. 1992 Fluid/kinetic hybrid moment description of plasmas via a chapmanenskoglike approach. *Phys. Fluids B: Plasma Phys.* **4**, 1139–1151.

WRIGHT, A. M. & FERRARO, N. M. 2024*a* Investigating nonlinear magnetohydrodynamics in an optimized, reactor-scale quasi-axisymmetric stellarator. *Phys. Plasmas* **31**, 082509.

WRIGHT, A. M. & FERRARO, N. M. 2024*b* MHD-induced beta limits in the large helical device. *Phys. Plasmas* **31**, 102509.

ZHOU, Y., FERRARO, N. M., JARDIN, S. C. & STRAUSS, H. R. 2021 Approach to nonlinear magnetohydrodynamic simulations in stellarator geometry. *Nucl. Fusion* **61**, 086015.